Atomic cluster expansion for a general-purpose interatomic potential of magnesium

Eslam Ibrahim,* Yury Lysogorskiy, Matous Mrovec, and Ralf Drautz†
ICAMS, Ruhr Universität Bochum, 44780 Bochum, Germany

(Received 6 May 2023; accepted 20 October 2023; published 17 November 2023)

We present a general-purpose parametrization of the atomic cluster expansion (ACE) for magnesium. The ACE shows outstanding transferability over a broad range of atomic environments and captures physical properties of bulk as well as defective Mg phases in excellent agreement with reference first-principles calculations. We demonstrate the computational efficiency and the predictive power of ACE by calculating properties of extended defects and by evaluating the $P-T$ phase diagram covering temperatures up to 3000 K and pressures up to 80 GPa. We compare the ACE predictions with those of other interatomic potentials, including the embedded-atom method, an angular-dependent potential, and a recently developed neural network potential. The comparison reveals that ACE is the only model among the tested potentials that is able to predict correctly the phase diagram in close agreement with experimental observations.

DOI: 10.1103/PhysRevMaterials.7.113801

I. INTRODUCTION

Magnesium is a lightweight and abundant metal, which makes it an attractive candidate material for automotive and aerospace components [1]. However, its low melting temperature and brittleness, attributed to the hexagonal close-packed (hcp) structure, limit the range of possible applications [2]. The hcp crystal structure of Mg as well as the body-centered cubic (bcc) structure of Na and the face-centered cubic (fcc) structure of Al, its neighbors in the periodic table, can be understood from the nearly free electron approximation [3]. In all these simple metals, the atomic cores induce Friedel oscillations in the electron density with characteristic wavelengths that depend on the Fermi energy and govern the stabilization of the bcc, hcp, and fcc crystal structures. Changes of the electronic structure under compression lead to various phase transitions [3,4]. While the phase diagram of Mg has been investigated both theoretically [5–10] and experimentally [11–15], exact locations of phase boundaries and existence of some phases are still under debate.

Atomistic simulations are nowadays indispensable for a detailed exploration of mechanical and thermodynamic properties. There exist several interatomic potentials for Mg, including embedded-atom method (EAM) potentials [16–20], modified embedded-atom method (MEAM) potentials [21–23], angular-dependent potentials (ADP) [24], tight-binding models [25,26], neural-network potentials (NNPs) [27,28], and a moment tensor potential (MTP) [29]. However, a recent study [30] showed that none of the potentials that were considered were able to predict accurately the $P-T$ phase diagram even for intermediate ranges of temperatures and pressures.

Here we present an interatomic potential for Mg that is able to describe reliably very different atomic configurations and is applicable to large-scale atomistic studies of mechanical as well as thermodynamic properties. The excellent transferability is achieved by parametrizing the atomic cluster expansion (ACE) [31] based on a wide range of density functional theory (DFT) reference data. We validate the potential in detail and demonstrate an excellent match to the reference data, in particular for properties that were not part of the training. We then apply the model to predict the Mg phase diagram.

The paper is structured as follows. In Sec. II we briefly review theoretical methods that we employ for the construction of ACE for Mg and for computations of mechanical and thermodynamic properties. In Sec. III we describe the ACE parametrization procedure. Section IV contains validation studies for fundamental structural, elastic and vibrational properties. In Sec. V we present the calculations of stacking faults and in Sec. VI we provide a comprehensive study of thermodynamic properties of Mg and evaluate the $P-T$ phase diagram using state-of-the-art thermodynamic integration techniques. Conclusions are provided in Sec. VII.

II. METHODS

A. DFT reference calculations

We employ the all-electron FHI-AIMS code [32,33] to carry out first-principles reference calculations based on density functional theory (DFT). All DFT calculations were performed using the Perdew-Burke-Ernzerhof (PBE) functional [34], tight basis settings, a k-mesh density of 0.175 $Å^{-1}$, and Gaussian smearing of 0.1 eV.

B. Atomic cluster expansion

The ACE parametrization was fitted using the package PACEMAKER [35]. We employed a Finnis-Sinclair-type mildly nonlinear representation of the atomic energy that

*eslam.saadibrahim@rub.de
†ralf.drautz@rub.de

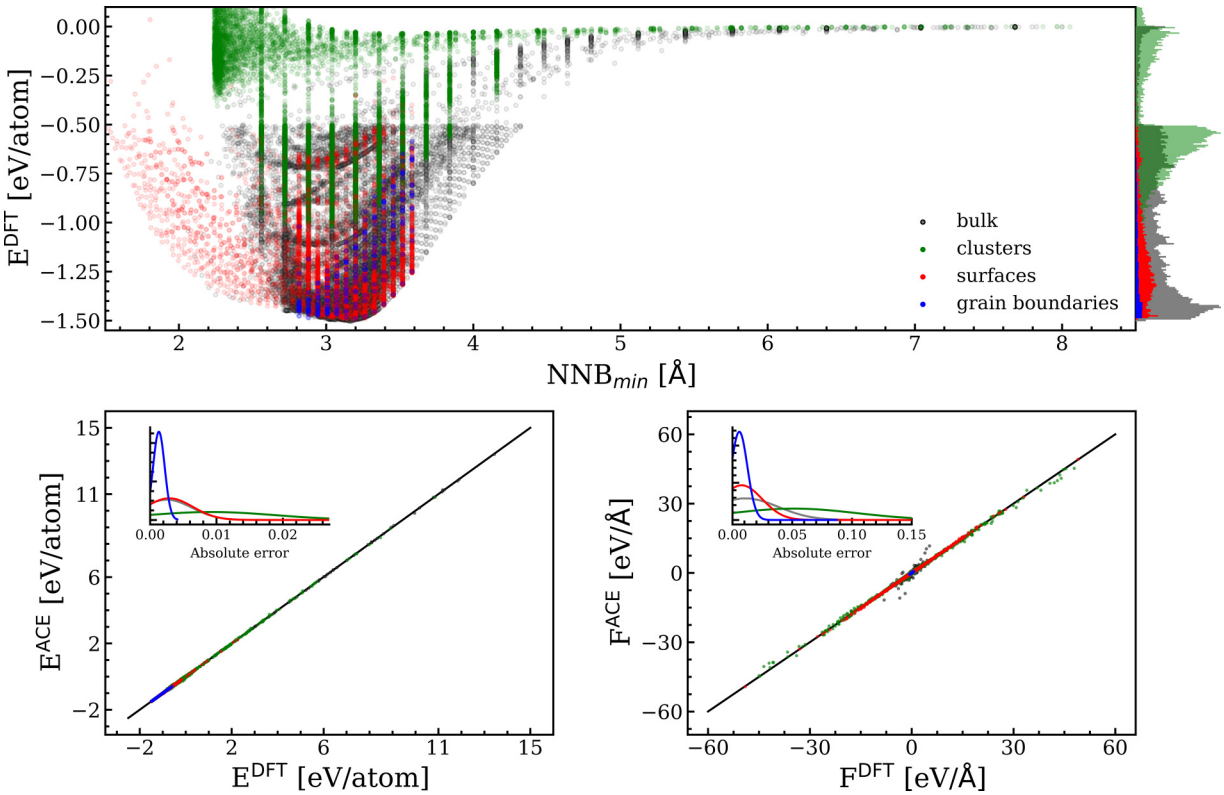

FIG. 1. DFT energies for the training dataset plotted with respect to the nearest neighbor distance in each structure (top panel). Cross-correlation plots and error distributions for energy and force showing an excellent agreement between ACE and DFT (bottom graphs).

incorporates two atomic properties that are represented by linear, in principle complete, ACE basis expansions [31,35,36]. The nonlinear representation can be motivated from the second-moment approximation [37] and was shown to be efficient [35] for metals [36] as well as covalently bonded materials [37,38]. A detailed description of the ACE methodology can be found in original Refs. [31,35,36,39,40].

C. Molecular dynamics and statics simulations

The Large-scale Atomic/Molecular Massively Parallel Simulator (LAMMPS) [41] and the Performant implementation of the atomic cluster expansion (PACE) [36] were used to carry out molecular statics and molecular dynamics (MD) simulations. Some calculations for other potentials were performed using the Atomic Simulation Environment (ASE) [42].

We calculated phonons using the force constants method as implemented in the PHONOPY package [43].

D. Computation of free energy

Nonequilibrium thermodynamic integration was used for free energy calculations as implemented in the software package CALPHY [44]. Two different integration paths were

TABLE I. Basic materials properties of the Mg hcp phase predicted by different interatomic potentials, DFT and experiment. The transformation pressure P_{tr} between the hcp and bcc phases at 0 K and the melting temperature T_m of the hcp phase are also included.

Property	DFT [50]	ACE	EAM [19]	ADP [24]	NNP [27]	Expt. [51]
a (Å)	3.190	3.187	3.185	3.188	3.186	3.209
c/a	1.627	1.623	1.628	1.633	1.613	1.624
C_{11} (GPa)	63.44	71.48	70.42	53.32	72.42	63.48
C_{12} (GPa)	26.15	24.30	25.56	16.74	30.31	25.94
C_{13} (GPa)	21.07	20.93	15.44	15.67	26.73	21.70
C_{33} (GPa)	68.47	67.14	69.05	73.62	68.22	66.45
C_{44} (GPa)	18.32	18.12	12.68	14.93	19.10	18.42
P_{tr} (GPa)	52.5[a]	51.6	33.9	22.6	5.5	≈ 50 [11]
T_m (K)		882 [b]	918[c]	910 [d]	≈ 900[e]	923

[a]We calculated this value using FHI-AIMS.
[b]Calculated from free energies with CALPHY.
[c]Calculated using solid-liquid interface free energy.
[d]Calculated using heating a crystal model with an open surface.
[e]Calculated using dual-phase crystal-liquid simulations.

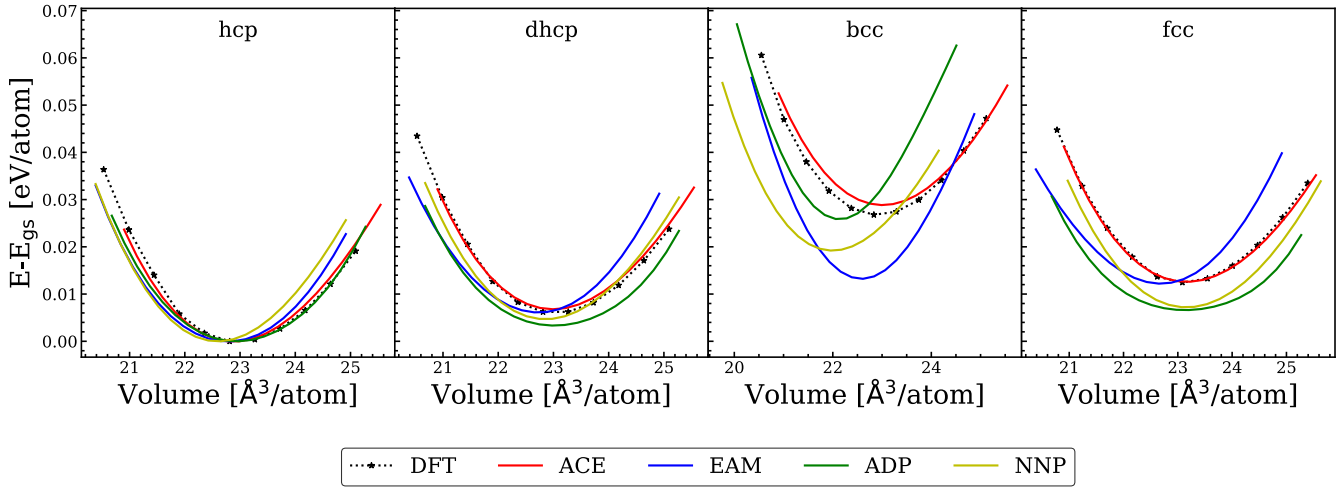

FIG. 2. Volume dependence of the energy for the most relevant Mg phases computed using ACE, EAM, ADP, NNP. and DFT. For each method, the energy of its equilibrium hcp structure was subtracted.

employed: the Frenkel-Ladd path [45] for computing the free energy at a given temperature and volume, and reversible scaling [46,47] for generating the free energy for a range of temperatures. We carefully converged the simulations to ensure free energy difference errors were significantly smaller than 1 meV (See Appendix A).

III. PARAMETRIZATION

We carried out more than 120 000 individual DFT reference calculations to sample local atomic environments as exhaustively as possible. The workflow management software PYIRON [48] was employed to automate some calculations. The atomic configurations comprised different bulk structures including supercells with displaced atoms, point defects, planar defects, and surfaces. In addition, we included small random clusters containing two to five atoms to ensure transferability to a large variety of atomic environments. We did not include any explicit information on liquid phases, but used active learning based on *D*-optimality [49] and principal component analysis to ensure that the reference data cover liquid phase atomic environments as discussed in Sec. VI. For the bulk phases, we sampled a range of volumes such that the nearest neighbor distances varied between about 0.7 and 3.0 of the nearest neighbor distance of the equilibrium hcp phase. The reference DFT data are plotted with respect to the nearest neighbor distance in each structure in the top panel of Fig. 1.

For the parametrization, we employed a successive hierarchical basis extension with power-order ranking [35] and a cutoff of 8.2 Å. From the full DFT reference dataset, we selected 40 000 structures for training (corresponding to 738 705 atoms) and 5000 structures for testing (corresponding to 92 900 atoms). The final ACE parametrization contained 724 basis functions and a total of 2528 parameters. Energies and forces in the structures were weighted using an energy based weighting scheme [35] that gave higher weights to low

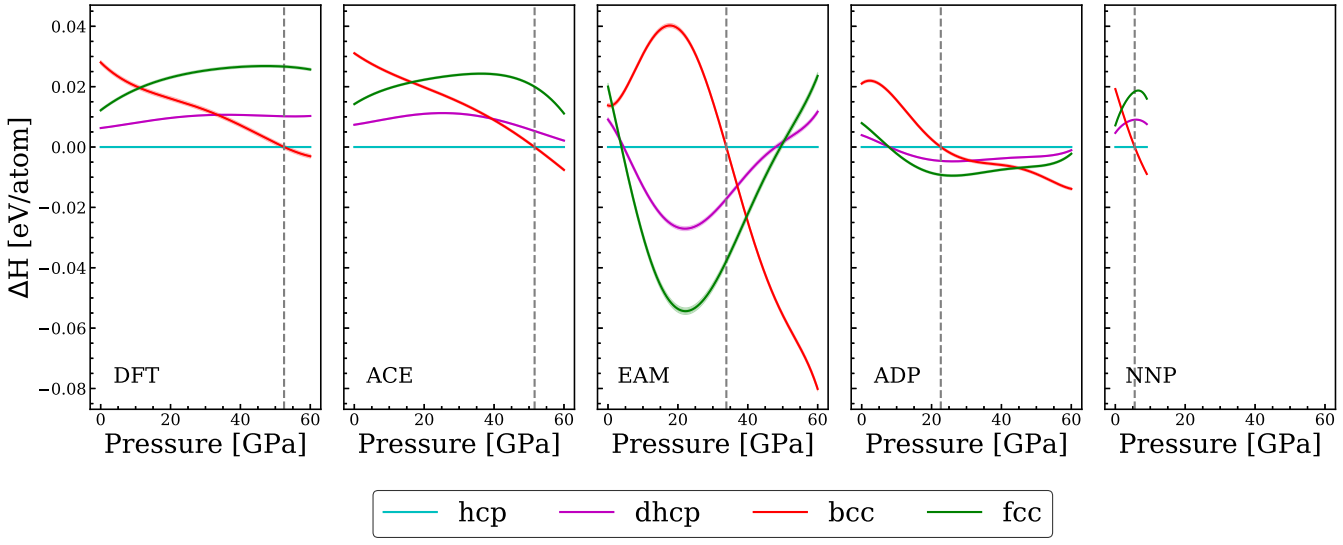

FIG. 3. Relative enthalpies (at 0 K) of the dhcp, bcc, and fcc phases with respect to that of the hcp phase as a function of pressure computed using ACE, EAM, ADP, NNP, and DFT.

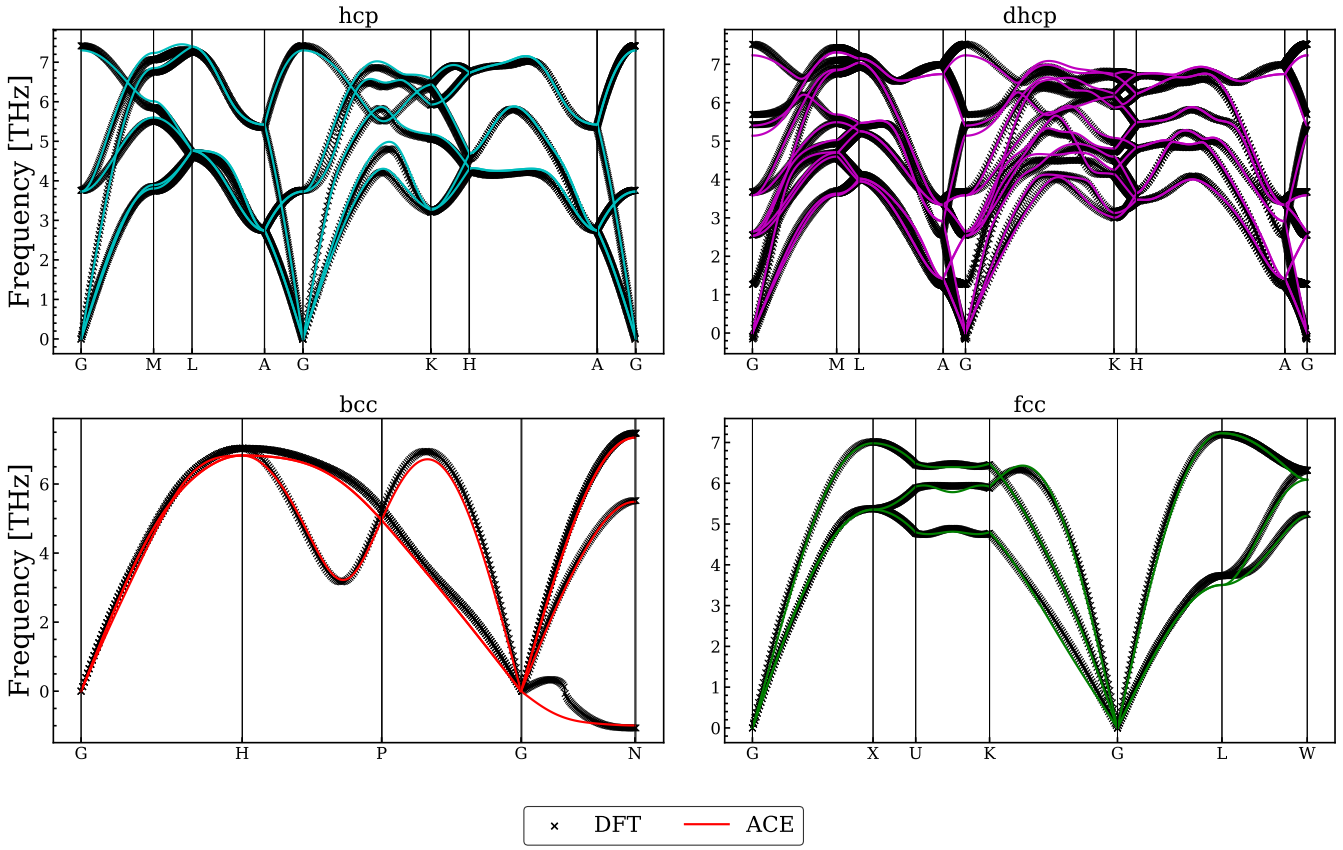

FIG. 4. Phonon band structures for hcp, dhcp, bcc, and fcc computed with ACE and DFT.

energy structures. Specifically, 75% of the weight was given to structures that were within 1 eV from the lowest energy structure.

Cross-correlation plots in Fig. 1 show that ACE reproduces the DFT reference data with excellent accuracy. The training metrics for the complete training set gives a mean-absolute error of 5.4 meV/atom for the energy and 31.5 meV/Å for the force. Corresponding errors for the test set of 5.7 meV/atom and 31.9 meV/Å, respectively, demonstrate that the model is not overfitted. Structures that are within 1 eV from the ground state were given the largest weight, and there errors are 4.7 meV/atom and 29.4 meV/Å for training and 4.9 meV/atom and 29.8 meV/Å for testing. Additional details of the training and error analysis are given in the Appendix A.

IV. VALIDATION

We validated the ACE parametrization by computing a number of materials properties. In addition, we compared ACE predictions with those of three other potentials for Mg, namely, an EAM potential developed for studies of solid-liquid interfaces [19], an ADP parametrization for pure Mg and the Mg-H system [24], and a recent NNP model aimed at studies of extended defects [27].

A. Equilibrium structure and elastic moduli

The equilibrium lattice constant a and the c/a ratio of the hcp phase at 0 K are reproduced by all potentials in close agreement with DFT and experiment (see Table I). The same holds for the elastic constants that are also summarized in Table I.

B. Structural stability and transition pressure

In Fig. 2, we compare the structural energies of the most relevant Mg phases—hcp, double hcp (dhcp), bcc, and fcc—computed using ACE, EAM, ADP, NNP, and DFT. ACE captures the structural energy differences in quantitative agreement with DFT for all considered phases while the other potentials show significant discrepancies for the bcc phase.

The energy difference between hcp and bcc is critical for the hcp-bcc phase transition. Figure 3 shows relative enthalpies of the bcc, fcc, and dhcp phases with respect to that of the hcp phase as a function of pressure, where we apply smoothing using a Savitzky-Golay filter as implemented in SCIPY [52]. It is apparent that only ACE agrees well with the DFT predictions while the other three potentials show not only quantitatively but even qualitatively incorrect behavior. The theoretically predicted transition pressures P_{tr} from hcp to bcc at zero temperature (marked by vertical dashed lines in Fig. 3) are 52.5, 51.6, 34.4, 23.7, and 5.5 GPa for DFT, ACE, EAM, ADP, and NNP, respectively. Our DFT and ACE values fall into the range of 47–55 GPa obtained by other electronic structure [7,8,50] and experimental [11,14,15] studies. Apart from quantitative discrepancies, EAM and ADP predict Mg to transform first to the fcc phase. The NNP model was trained mostly on structures close to the equilibrium densities and

TABLE II. Calculated surface energies (in eV/Å^2) for hcp and bcc phases. The DFT values are taken from the Crystalium database [53–55].

hcp	ACE	DFT	bcc	ACE	DFT
(0001)	0.034	0.032	(111)	0.041	0.047
(10$\bar{1}$0)	0.036	0.037	(211)	0.028	0.030
(10$\bar{1}$1)	0.047	0.039	(321)	0.028	0.030
(21$\bar{3}$0)	0.040	0.044	(110)	0.033	0.037
(10$\bar{1}$2)	0.049	0.044	(320)	0.048	0.038
(11$\bar{2}$0)	0.041	0.045	(210)	0.026	0.039
(21$\bar{3}$1)	0.040	0.046	(310)	0.033	0.039
(21$\bar{3}$2)	0.050	0.046	(331)	0.041	0.041
(2$\bar{1}\bar{1}$2)	0.053	0.046	(322)	0.050	0.043
(22$\bar{4}$1)	0.041	0.047	(311)	0.042	0.044
(11$\bar{2}$1)	0.039	0.047	(100)	0.058	0.044
(20$\bar{2}$1)	0.035	0.048	(221)	0.063	0.047
			(332)	0.055	0.048

therefore is unable to predict correctly the behavior at elevated pressures.

C. Phonon spectra

In Fig. 4, we present the computed phonon band structures for hcp, dhcp, bcc, and fcc using ACE and DFT. We observe very close agreement between ACE and DFT, including the prediction of negative phonons in bcc. In Appendix A, we compare the phonon density of states for the tested interatomic potentials, which demonstrates significant deviation from the DFT reference. For example, for bcc, one can see that ACE is the only potential that aligns well with the DFT predictions. Neither EAM nor ADP predict negative phonons in the bcc phase, in contrast to ACE and NNP. This can be related to relative phase stabilities. In Fig. 3 we show the enthalpy of formation for DFT, ACE, and the other potentials. ACE and NNP show a transition between hcp and bcc, while for EAM and ADP the fcc phase appears, in disagreement also with the DFT reference.

D. Surface energies

We calculated energies of various surfaces of Mg in the hcp and bcc phases, as displayed in Table II. The atomic configurations and DFT data were taken from the Crystalium database [53–55]. The surfaces of the hcp phase were not part of the training reference data. Hence, the prediction of surface energies presents a stringent test of the ACE transferability. For hcp, the close-packed (0001) surface has the lowest energy with a deviation between ACE and DFT of only 2 meV/Å^2. Other surfaces are reproduced equally well or with only slightly larger errors.

E. Transformation paths

Along transformation paths between crystal structures, coordination and bond distances change significantly. To illustrate the capability of ACE to describe large bonding rearrangements, we calculated the energy along four different transformation paths. In Fig. 5, we show the trigonal, hexagonal, tetragonal, and orthorhombic paths as predicted by ACE and DFT. The discontinuities that are visible in the DFT data of the orthorhombic path are due to k-point

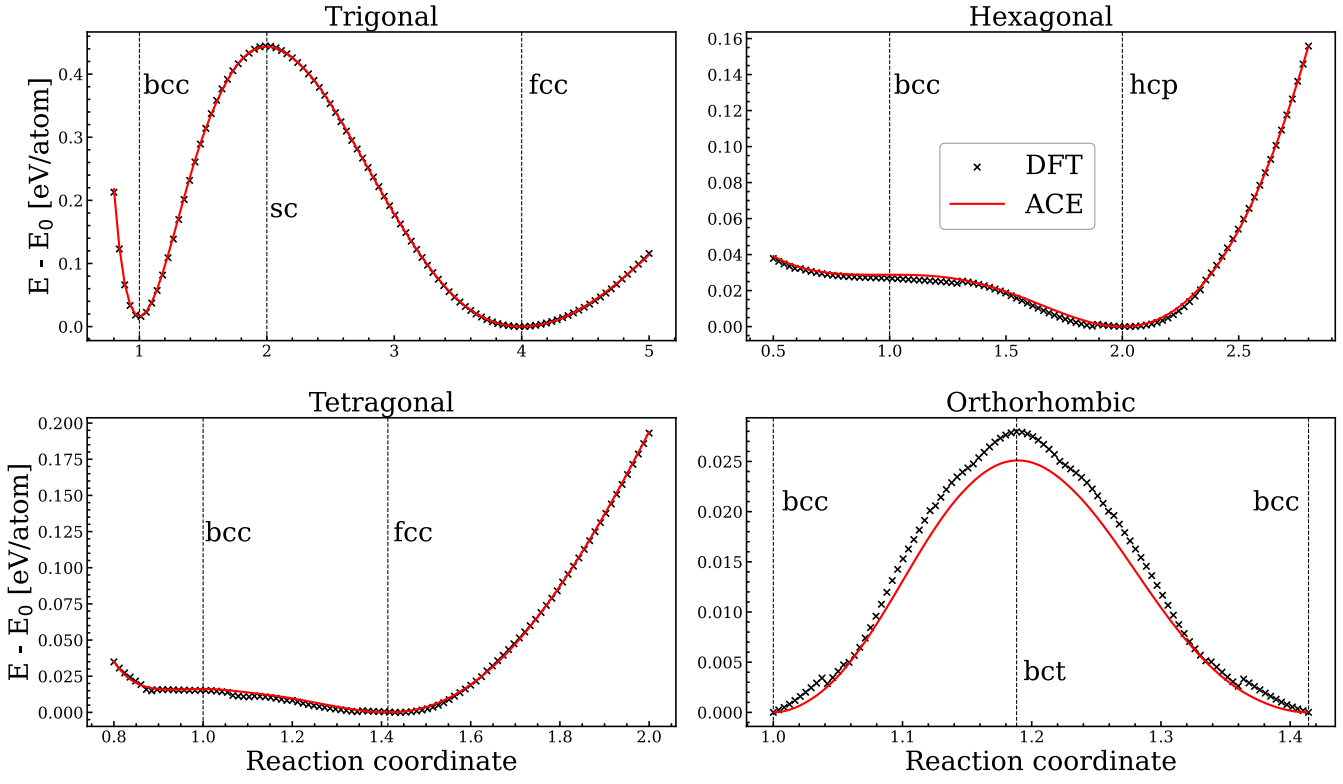

FIG. 5. Trigonal, hexagonal, tetragonal, and orthorhombic transformation paths for ACE and DFT.

TABLE III. Stacking fault (SF) energies (in mJ/m^2) calculated by ACE and DFT [63]. The acronyms ISF and ESF correspond to intrinsic and extrinsic faults, respectively; the letters N and W mark narrow and wide atomic planes (see text); for a detailed description of SF configurations see Ref. [63].

	ACE	DFT
Basal		
ISF1	25	18
ISF2	49	34
ESF	72	54
Prismatic I		
W-SF1	201	212
W-SF2	363	383
Prismatic II		
SF1	206	183
Pyramidal I		
N-SF1	169	165
W-SF1	285	-
W-SF2	158	161
W-SF3	232	203
Pyramidal II		
SF1	185	165

remeshing. Results for the other potentials are provided in the Appendix A.

V. STACKING FAULTS AND GENERALIZED STACKING FAULT ENERGY SURFACES

The low ductility of Mg at ambient temperatures is related to a limited number of available slip systems [1,56]. The close-packed basal plane offers two independent primary slip systems where the $\langle a \rangle$ dislocations glide at relatively low stresses [57,58]. To initiate plasticity during loading along the $\langle c \rangle$ axis necessitates glide of $\langle c + a \rangle$ dislocations on secondary pyramidal slip systems. This usually requires a thermal activation and elevated stresses [1,2,59–62].

Generalized stacking fault energy (GSFE) surfaces, also known as γ-surfaces [64], are an important indicator for dislocation behavior. Since they are accessible by first principles calculations [63,65–70] and experiments [71–73], they can be used also for validation of interatomic potentials. It has been reported [67,74] that there exist notable differences in GSFE values obtained by DFT and EAM potentials.

We calculated energies of stable stacking faults on the basal {0001}, prismatic I $\{10\bar{1}0\}$, prismatic II $\{11\bar{2}0\}$, pyramidal I $\{10\bar{1}1\}$, and pyramidal II $\{11\bar{2}2\}$ planes and compared them to results of a recent DFT study [63]. The comparison in Table III

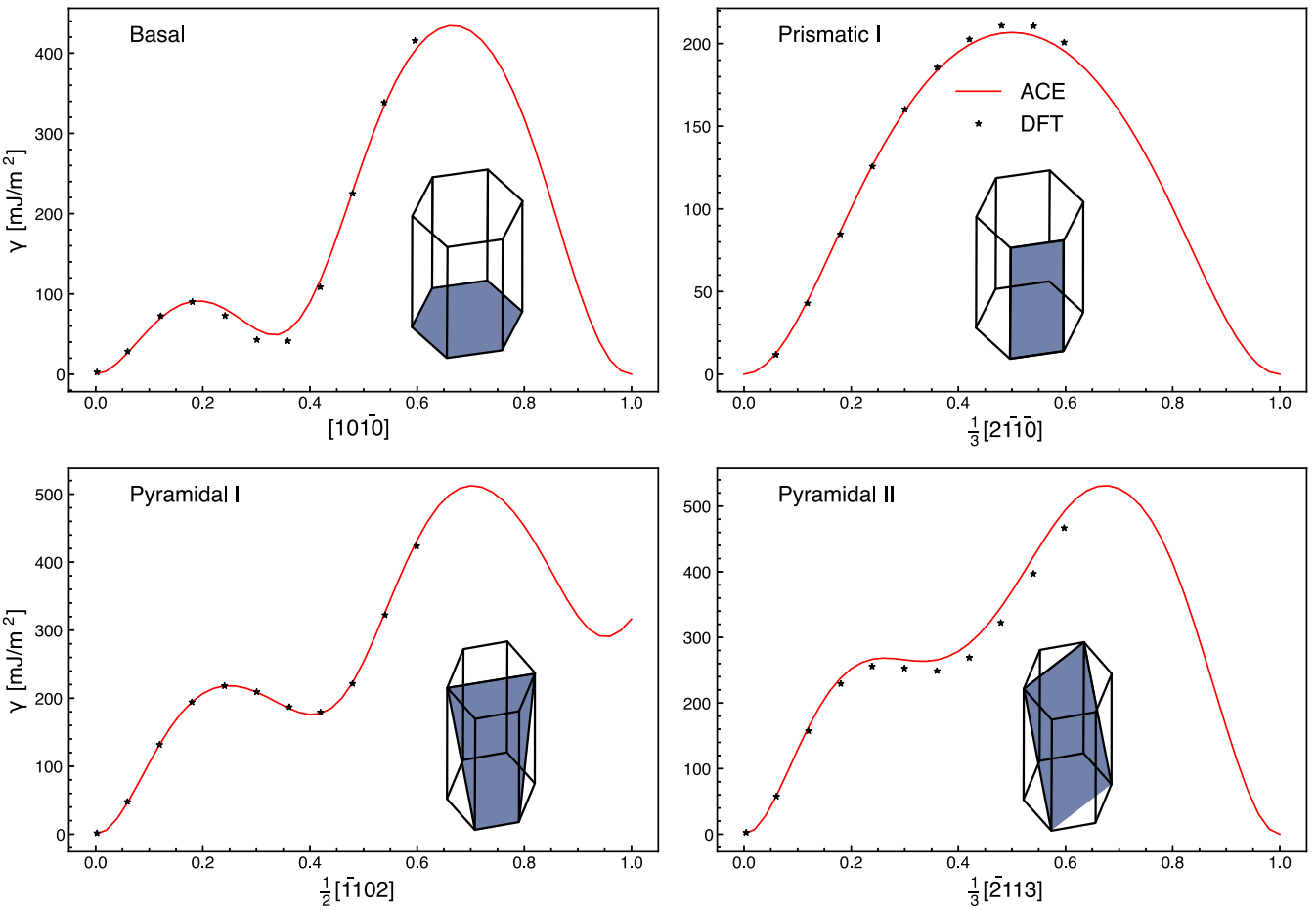

FIG. 6. Generalized stacking fault energy γ lines on several planes in hcp Mg. Panels show data for the basal, prismatic I, pyramidal I, and pyramidal II planes from ACE and DFT [63].

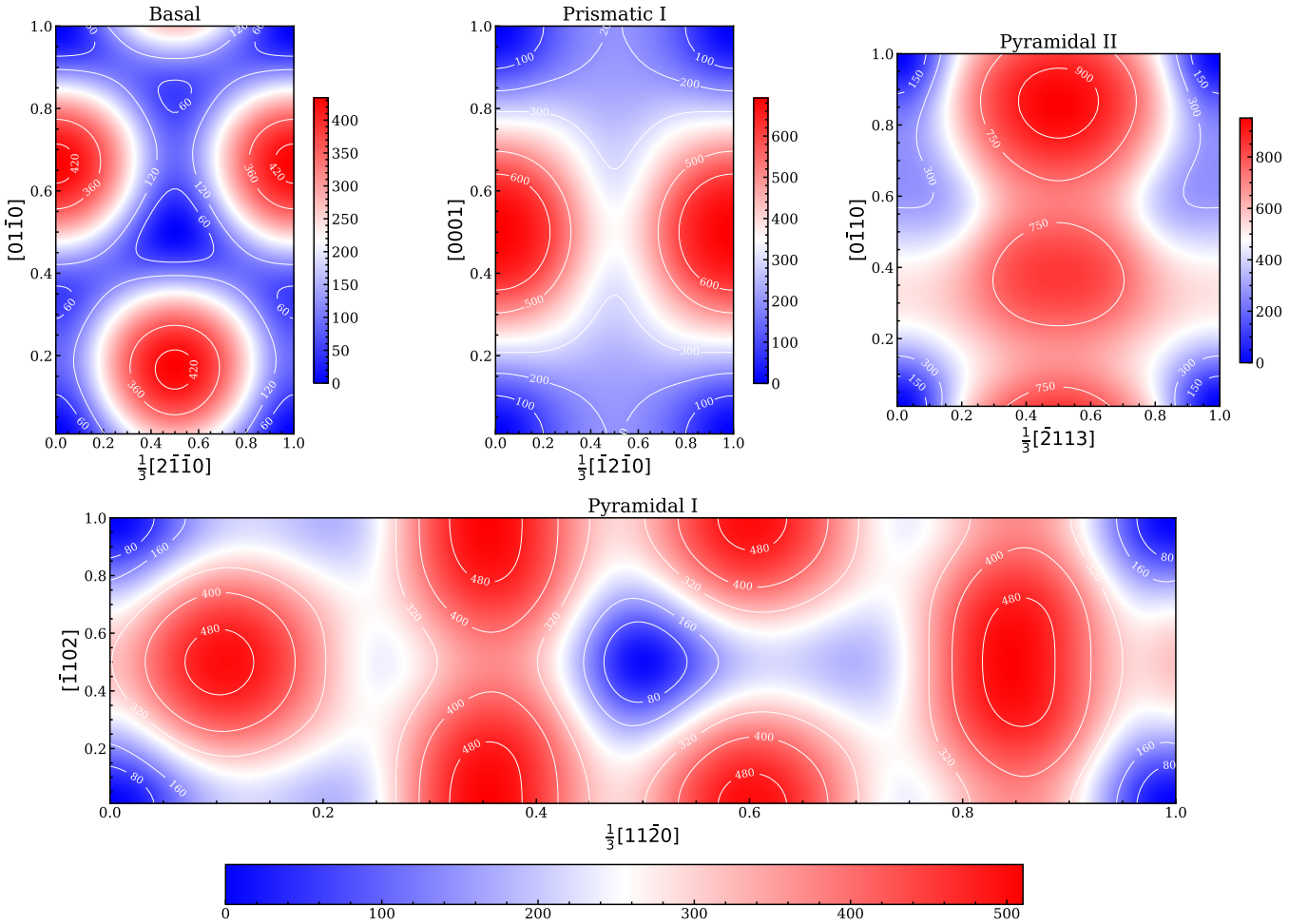

FIG. 7. The generalized stacking fault energy (γ-surface) on several planes in hcp Mg. Panels show the data for the basal, prismatic I, pyramidal I, and pyramidal II planes calculated using ACE.

shows a good agreement for all stacking faults with errors not exceeding 30 mJ/m^2. It is important to note that none of the faults were included in the training data.

Apart from the stable stacking faults, we calculated entire γ-surfaces for the basal $\{0001\}$, prismatic I $\{10\bar{1}0\}$, prismatic II $\{11\bar{2}0\}$, pyramidal I $\{10\bar{1}1\}$, and pyramidal II $\{11\bar{2}2\}$ planes. In Fig. 6, we show first cross sections of the γ-surfaces along high symmetry directions that are relevant for splitting of dislocation cores. The plots contain also DFT results from Ref. [63]. Overall, ACE shows an excellent agreement with DFT for all investigated directions. From the cross section on the basal plane one can see that not only the stable but also the unstable stacking fault energy, corresponding to the shift of about $\frac{1}{6}[10\bar{1}1]$, is reproduced very accurately and is consistent with existing DFT data [66,74]. The same applies also for both pyramidal planes.

Contour plots of the entire γ-surfaces are shown in Fig. 7. The γ-surfaces for the basal and prismatic planes agree well with available DFT results [68]. A single metastable stacking fault (I2) is visible on the basal plane and none are visible on the prismatic planes.

For the first-order pyramidal I $\{10\bar{1}1\}$ plane, there exist two sets of atomic layers with narrow (N) and wide (W) spacings between them. Here we evaluated the γ-surface between the widely spaced planes that is relevant for the splitting of the $\langle c+a \rangle$ dislocations. The shapes of of both pyramidal γ-surfaces as well as the locations of the stacking faults agree quantitatively with values reported in recent DFT studies on Mg [61,63,75] and are also consistent with DFT results for hcp metals Ti [76] and Zr [77].

VI. PHASE DIAGRAM

An evaluation of phase diagram using DFT calculations is computationally expensive so that accurate and efficient interatomic potentials are largely beneficial for such a task. However, a recent comparative study [30] revealed that none of the potentials considered, including several EAM [16–20] and MEAM [21–23] potentials, ADP [24], tight-binding models [25,26], and NNPs [27,28], were able to provide a satisfactory description of thermodynamic properties of Mg over a broad range of temperatures and pressures.

We computed the $P-T$ phase diagram using nonequilibrium thermodynamic integration (NETI) [78], where we employed two thermodynamic paths: the Frenkel-Ladd path [45] and the reversible-scaling path [46,47]. For the automated calculations of the Gibbs free energies of all phases we used the software package CALPHY [44]. Examples of the Gibbs

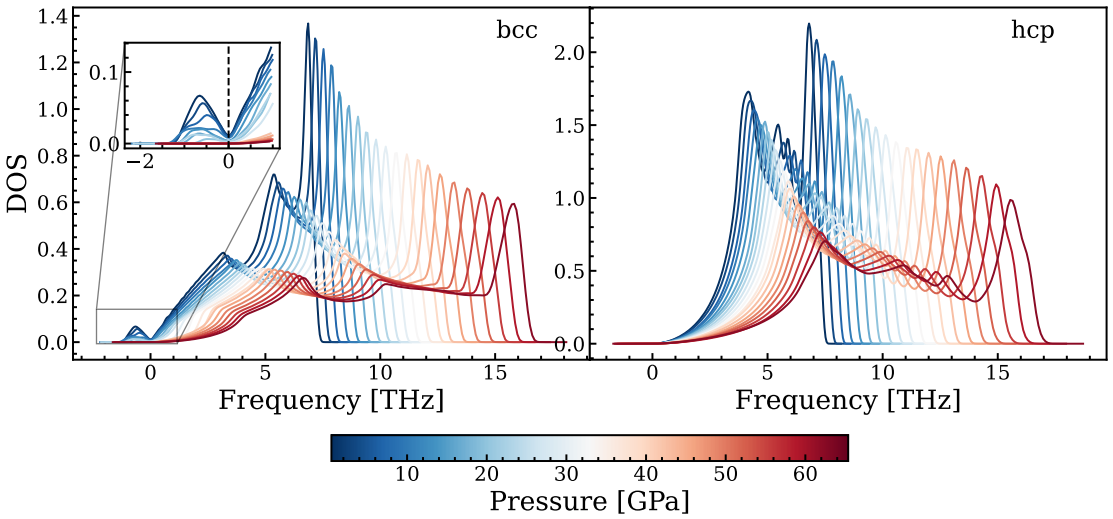

FIG. 8. Phonon densities of states of the hcp and bcc phases at different pressures as predicted by ACE.

free energies at zero pressure computed using NETI for different temperatures together with additional convergence studies are provided in the Appendix B.

The complete phase diagram predicted by ACE is presented in Fig. 9. For the investigated range of temperatures and pressures, there exist only three phases, namely, hcp, bcc, and liquid. It should be noted that the DFT training data did not contain any configurations at extreme densities and energies so that the present ACE parametrization is reliable up to pressures of about 70 GPa and temperatures up to about 4000 K only.

The liquidus line predicted by ACE shows a good agreement with the experimental data [10,12,14,15] as well as recent AIMD results [10] despite the fact that no liquid reference DFT data were included in the training procedure. In order to validate that the liquid environments are captured reliably by ACE, we computed the uncertainty indicator γ [49] to estimate the extrapolation grade in the description of the local atomic environments occurring in the liquid phase. A value of γ between 0 and 1 indicates interpolation, i.e., reliable prediction, while $\gamma > 1$ corresponds to extrapolation and increasingly uncertain predictions. Furthermore, we carried out principal component analysis (PCA) of the ACE basis function for the training configurations as well as for the liquid configurations obtained during the phase diagram simulations up to 13 GPa. In Fig. 10, we show first two components of PCA decomposition together with the extrapolation grade obtained for the liquid structures. It can be seen that the extrapolation grade is smaller than 1 for most liquid configurations and that the liquid local atomic environments overlap with the environments in the training dataset. This analysis demonstrates that atomic configurations found in the liquid were efficiently sampled during training, despite the fact that explicitly liquid configurations, for example, from AIMD, were not part of the training set.

The region of the phase diagram in the vicinity of the triple point is still rather uncertain. There exists evidence of additional diffraction peaks [12,14] that do not belong to hcp, dhcp, or bcc phases, but no other crystalline phase could be identified so far. According to recent shock-release experiments, the triple point of polycrystalline Mg lies at about 20 GPa and 1650 K [15], which is higher than most theoretical estimates.

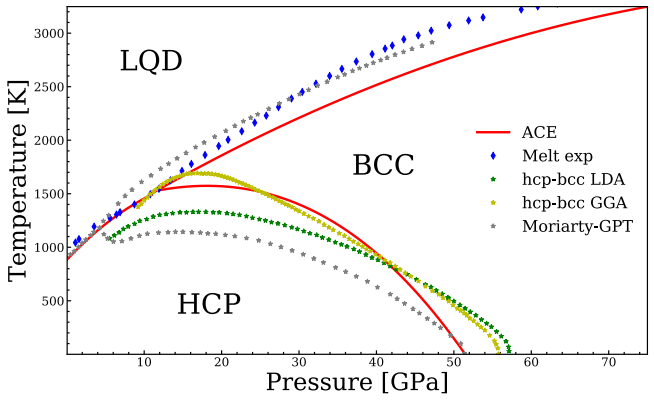

FIG. 9. Mg phase diagram predicted by ACE together with results from literature from experimental [12], as well as theoretical studies [7,8].

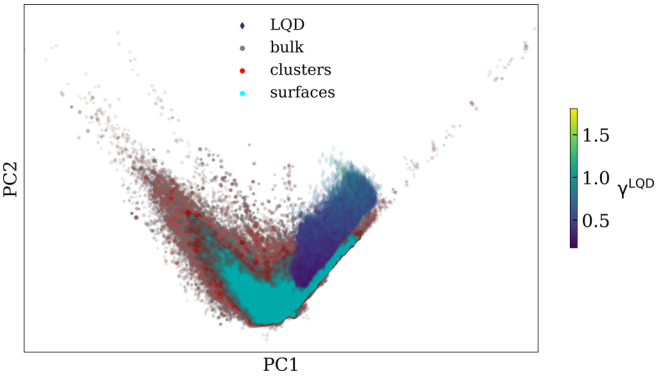

FIG. 10. PCA of the *B*-basis function projections for training set and liquid local atomic environments, which were not part of the training.

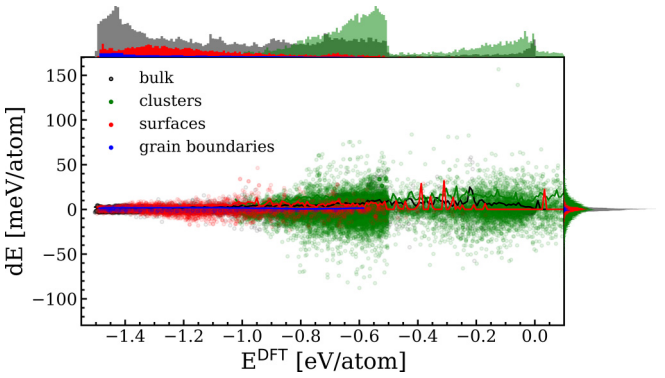

FIG. 11. Error in the energy per atom as a function of the reference DFT energy for the training dataset. The solid lines show the average RMSE, the top panel shows the number of samples, and the right panel the overall error distribution.

To analyze in more detail the origins of the hcp-bcc transformation, we evaluated the phonon density of states for both phases as a function of pressure, as shown in Fig. 8. We find that hcp is dynamically stable at all pressures while the bcc phase is unstable below 30 GPa, as evidenced by the negative phonon frequencies. The dynamical instability of the bcc phase at low pressures is consistent with available DFT results [4,7,8,50,79] This instability is caused by an unstable transverse phonon mode at the bcc N-point zone boundary and is directly related to the mechanism of the martensitic hcp-bcc phase transformation [79].

VII. CONCLUSION

We developed a general-purpose interatomic potential for Mg based on the atomic cluster expansion. The present ACE parametrization predicts materials properties with accuracy similar to the DFT reference for a broad range of atomic environments. We demonstrated the broad applicability of the ACE model by analyzing properties of extended defects and evaluated the $P-T$ phase diagram of Mg over an extensive range of temperatures and pressures.

The DFT reference data and the potential are available online [80].

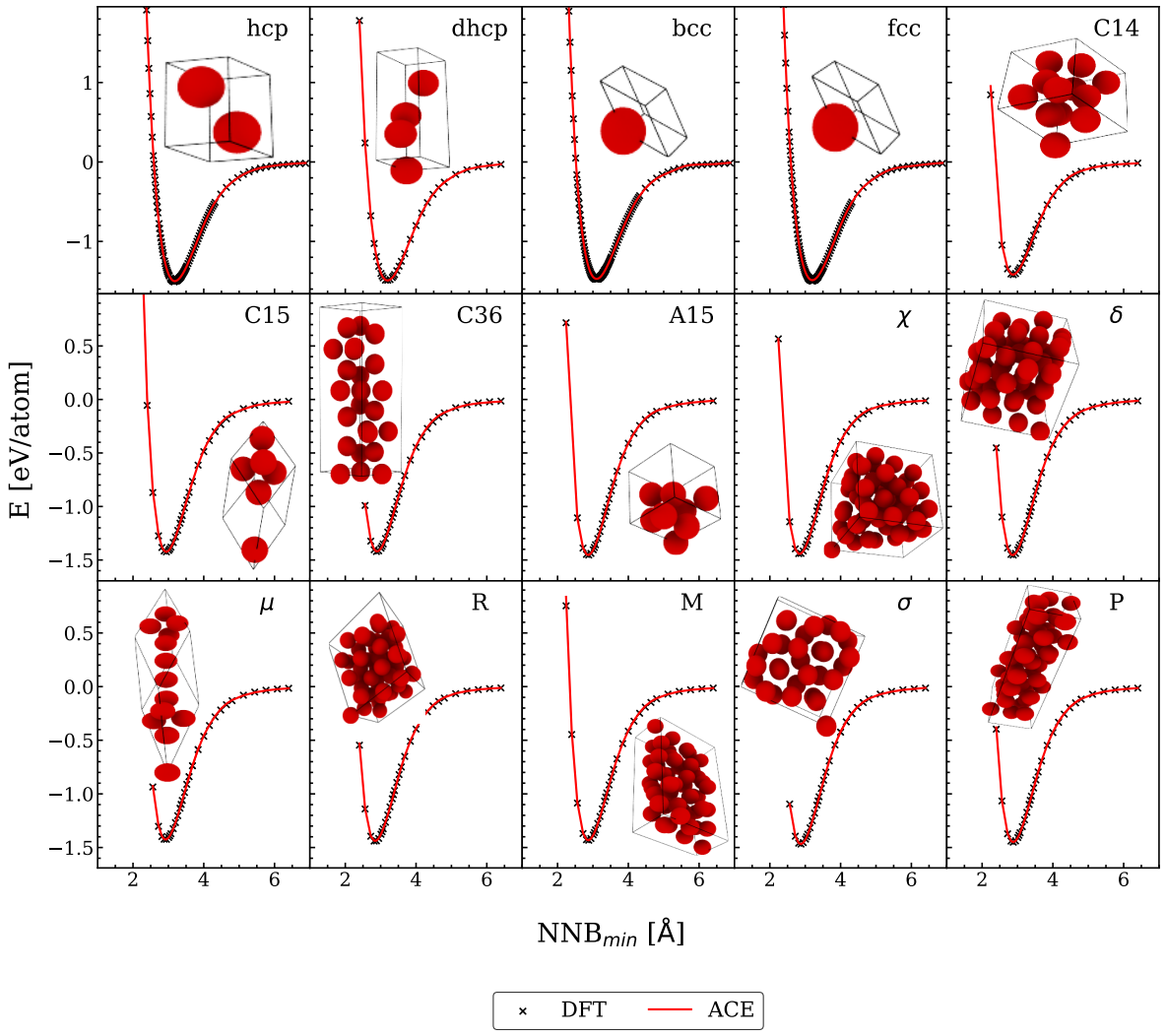

FIG. 12. Energy with respect to nearest neighbor distance for selected bulk structures.

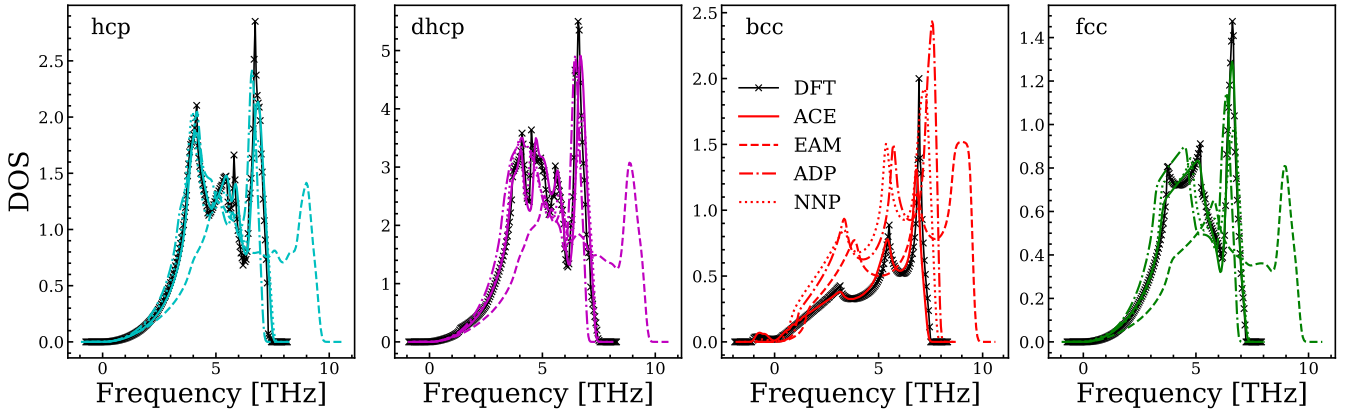

FIG. 13. Phonon DOS for hcp, dhcp, bcc, and fcc computed with DFT, ACE, EAM, ADP, and NNP.

ACKNOWLEDGMENTS

E.I. acknowledges funding through the International Max Planck Research School for Sustainable Metallurgy (IMPRS SusMet). We acknowledge computational resources from the research center ZGH at Ruhr-University Bochum.

APPENDIX A: ADDITIONAL VALIDATION RESULTS

Our training dataset contains various structures including bulk, surfaces, grain boundaries, clusters, and various shaken and random structures. In Fig. 12, we show energy versus nearest neighbor distance (NNB_{min}) for additional bulk structures calculated using ACE and DFT. The results demonstrate a close agreement between ACE and the DFT reference. In addition, one can see that the ACE curves are smooth over the whole range of NNB_{min}, which is not straightforward to achieve.

In Fig. 11, we provide an additional quantification of the ACE errors and their distribution with respect to the DFT reference.

In Fig. 13, we show a comparison of phonon density of states (DOS) calculated using DFT, ACE, and the considered interatomic potentials for four most relevant structures (hcp, dhcp, bcc, and fcc). Only ACE correctly predicts imaginary

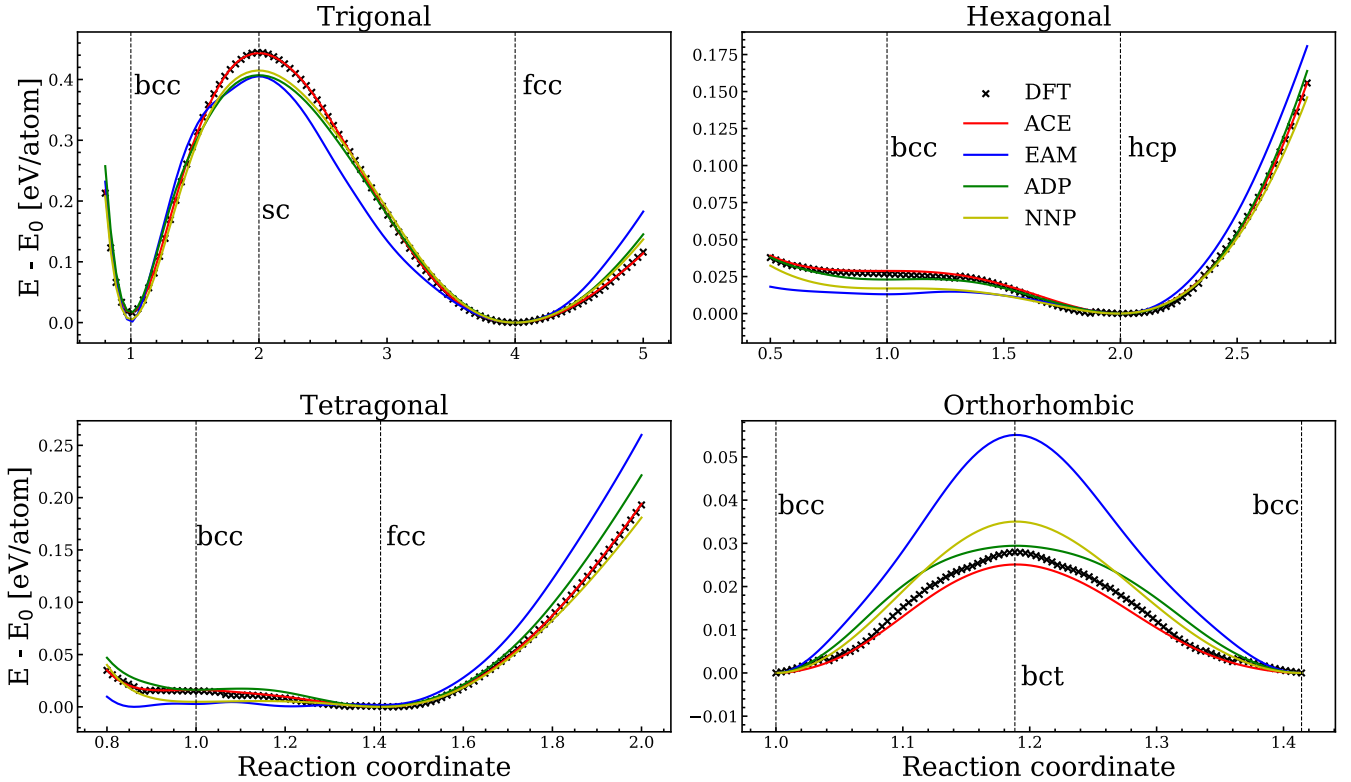

FIG. 14. Transformation paths for trigonal, hexagonal, tetragonal, and orthorhombic paths computed with DFT, ACE, EAM, ADP, and NNP.

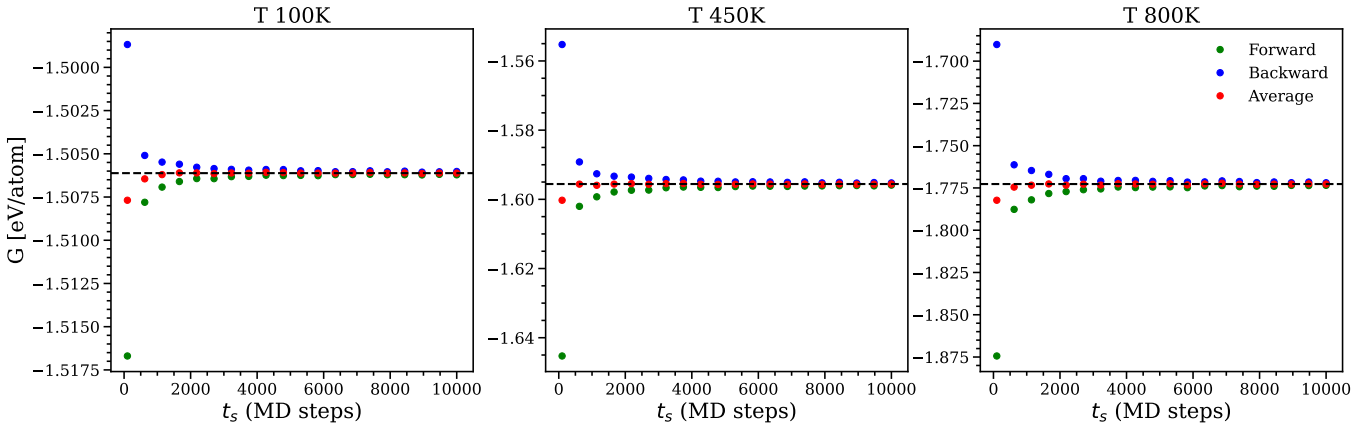

FIG. 15. FL NETI results for the forward direction, backward direction, and their average for three different temperatures. The dashed line shows the value at the thermodynamic limit. The averaged path converges much faster than the forward and backward directions, showing the efficiency of the NETI scheme.

phonon frequencies in the case of bcc in accordance with DFT, while EAM and ADP predict the bcc structure to be dynamically stable.

The transformation paths for all considered interatomic potentials are compared in Fig. 14.

APPENDIX B: FREE ENERGY

Here, we discuss the implementation and calculations of free energies using NETI. Figure 15 shows the Gibbs free energies at zero pressure computed using NETI for three different temperatures, 100, 400, and 800 K. The x axis shows the switching time in terms of MD steps, where one MD step corresponds to 2 fs. We employ the Frenkel-Ladd (FL) calculations in three directions, namely, forward, backward, and average. The average indicates the average of forward and backward switching. Then, we average the results of both of them. The dashed line shows the free energy in the thermodynamic limit for each corresponding temperature. Here one sees that the average direction converges more rapidly than the forward and backward directions. This behavior explains how the heat of dissipation decreases differently with the different paths. Figure 15 shows that one obtains excellent free energy estimation within a few hundred MD steps. However, one gets the same accuracy of the average direction using either forward or backward direction within a few thousand MD steps. Irrespective of the simulation temperature, we see a typical behavior of free energy convergence. Naturally, the absolute values of the converged free energies are different for different temperatures. From another point of view, one can relate this to the rate of termination at which we carry out our process. Hence, one arrives at almost negligible heats of dissipation with the average direction at higher rates in comparison to either the forward or the backward direction, leading to a more computationally efficient way. In principle, this for two reasons. First, we terminate the process at a relatively long switching time. Second, we average the forward and backward processes, which have almost the same heats of dissipation even at shorter switching times. Thus, as we increase the switching time (i.e., decrease the rate at which we terminate our process.), we get smaller heats of dissipation from the forward and backward directions.

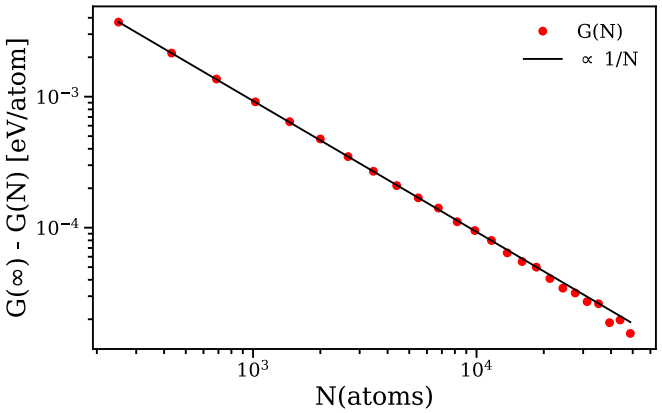

FIG. 16. We obtained an estimate for the Gibbs free energy in the thermodynamic limit, $G(\infty)$, by making an asymptotic analysis which has shown that the free energy, $G(N)$, converges with the leading term $1/N$.

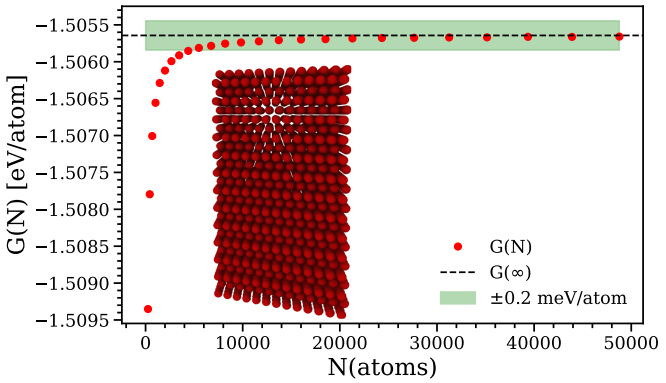

FIG. 17. Free-energy convergence with the system size for the hcp structure at 100 K and zero pressure. The chosen accuracy was within ± 0.2 meV/atom of the free energy in the thermodynamic limit.

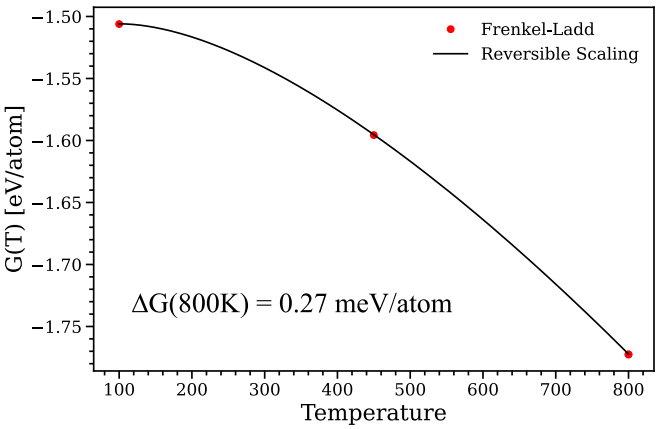

FIG. 18. Gibbs free energy of the hcp structure calculated using the ACE potential. The reference free energy from the FL thermodynamic path is at $T_0 = 100$ K and zero pressure. The FL calculations at other temperatures were used to verify the agreement against the RS result at high temperatures.

Another convergence test that we carried out is the behavior of the free energy as a function of the system size. Figure 17 shows a typical convergence behavior for the free energy as a function of the number of atoms or the system size. One sees that, for a small number of atoms ($\lesssim 200$), deviations are high and cannot be ignored. However, for larger systems, the deviations are insignificant (<1 meV) and can be disregarded. In these analyses, we use the hcp lattice of Mg and we vary the dimensions $N \times N \times N$ of the supercell where $N = 5, 6, 7, \ldots, 29$. This results in supercells containing from 250 to 48778 atoms. From these results, one sees that attaining a convergence of the free energy within a fraction of meV demands a few thousand atoms, where we calculate the value of free energy at the thermodynamic limit as shown in Fig. 16.

Figure 18 shows the free energies from the FL and reversible scaling (RS) thermodynamic paths at zero pressure. We calculate the free energies using FL and RS thermodynamic paths in a temperature range from 100 to 800 K (slightly below the melting point). Red points show single calculations of the free energies at temperatures of 100, 450, and 800 K using FL thermodynamic path. The solid line shows the results of the free energies using the RS thermodynamic path with a reference point from FL free energy at 100 K. In principle, RS calculations require a larger switching time to achieve similar accuracy as FL calculations. A typical FL switching time to reach convergence of a fraction of meV is around 5000 MD steps, where an MD step corresponds to 2 fs. A typical RS switching time is around 25 000 MD steps.

[1] B. Mordike and T. Ebert, Mater. Sci. Eng., A **302**, 37 (2001).
[2] Z. Wu and W. Curtin, Nature (London) **526**, 62 (2015).
[3] D. G. Pettifor, *Bonding and Structure of Molecules and Solids* (Oxford University Press, Oxford, 1995).
[4] G. Grimvall, B. Magyari-Köpe, V. Ozoliņš, and K. A. Persson, Rev. Mod. Phys. **84**, 945 (2012).
[5] A. K. McMahan and J. A. Moriarty, Phys. Rev. B **27**, 3235 (1983).
[6] A. McMahan, Physica B+C **139-140**, 31 (1986).
[7] J. A. Moriarty and J. D. Althoff, Phys. Rev. B **51**, 5609 (1995).
[8] S. Mehta, G. Price, and D. Alfè, J. Chem. Phys. **125**, 194507 (2006).
[9] P. Li, G. Gao, Y. Wang, and Y. Ma, J. Phys. Chem. C **114**, 21745 (2010).
[10] C. Cui, J. Xian, H. Liu, F. Tian, X. Gao, and H. Song, J. Appl. Phys. **131**, 195901 (2022).
[11] H. Olijnyk and W. B. Holzapfel, Phys. Rev. B **31**, 4682 (1985).
[12] D. Errandonea, R. Boehler, and M. Ross, Phys. Rev. B **65**, 012108 (2001).
[13] D. Errandonea, Y. Meng, D. Häusermann, and T. Uchida, J. Phys.: Condens. Matter **15**, 1277 (2003).
[14] G. W. Stinton, S. G. MacLeod, H. Cynn, D. Errandonea, W. J. Evans, J. E. Proctor, Y. Meng, and M. I. McMahon, Phys. Rev. B **90**, 134105 (2014).
[15] M. T. Beason, B. J. Jensen, and S. D. Crockett, Phys. Rev. B **104**, 144106 (2021).
[16] X.-Y. Liu and J. B. Adams, Acta Mater. **46**, 3467 (1998).
[17] X. W. Zhou, R. A. Johnson, and H. N. G. Wadley, Phys. Rev. B **69**, 144113 (2004).
[18] D. Y. Sun, M. I. Mendelev, C. A. Becker, K. Kudin, T. Haxhimali, M. Asta, J. J. Hoyt, A. Karma, and D. J. Srolovitz, Phys. Rev. B **73**, 024116 (2006).
[19] S. Wilson and M. Mendelev, J. Chem. Phys. **144**, 144707 (2016).
[20] Z. Pei, H. Sheng, X. Zhang, R. Li, and B. Svendsen, Mater. Des. **153**, 232 (2018).
[21] Y.-M. Kim, N. J. Kim, and B.-J. Lee, Calphad **33**, 650 (2009).
[22] D. E. Dickel, M. I. Baskes, I. Aslam, and C. D. Barrett, Modell. Simul. Mater. Sci. Eng. **26**, 045010 (2018).
[23] R. Ahmad, Z. Wu, and W. Curtin, Acta Mater. **183**, 228 (2020).
[24] D. Smirnova, S. Starikov, and A. Vlasova, Comput. Mater. Sci. **154**, 295 (2018).
[25] F. Cleri and V. Rosato, Phys. Rev. B **48**, 22 (1993).
[26] X. Li, Y. Qin, J. Fu, and J. Zhao, Comput. Mater. Sci. **98**, 328 (2015).
[27] M. Stricker, B. Yin, E. Mak, and W. A. Curtin, Phys. Rev. Mater. **4**, 103602 (2020).
[28] D. Dickel, M. Nitol, and C. Barrett, Comput. Mater. Sci. **196**, 110481 (2021).
[29] M. Poul, L. Huber, E. Bitzek, and J. Neugebauer, Phys. Rev. B **107**, 104103 (2023).
[30] J. F. Troncoso and V. Turlo, Modell. Simul. Mater. Sci. Eng. **30**, 045009 (2022).
[31] R. Drautz, Phys. Rev. B **99**, 014104 (2019).
[32] V. Blum, R. Gehrke, F. Hanke, P. Havu, V. Havu, X. Ren, K. Reuter, and M. Scheffler, Comput. Phys. Commun. **180**, 2175 (2009).
[33] V. Havu, V. Blum, P. Havu, and M. Scheffler, J. Comput. Phys. **228**, 8367 (2009).
[34] J. P. Perdew, K. Burke, and M. Ernzerhof, Phys. Rev. Lett. **77**, 3865 (1996).
[35] A. Bochkarev, Y. Lysogorskiy, S. Menon, M. Qamar, M. Mrovec, and R. Drautz, Phys. Rev. Mater. **6**, 013804 (2022).

[36] Y. Lysogorskiy, C. v. d. Oord, A. Bochkarev, S. Menon, M. Rinaldi, T. Hammerschmidt, M. Mrovec, A. Thompson, G. Csányi, C. Ortner *et al.*, npj Comput. Mater. **7**, 97 (2021).

[37] M. Qamar, M. Mrovec, Y. Lysogorskiy, A. Bochkarev, and R. Drautz, Atomic cluster expansion for quantum-accurate large-scale simulations of carbon, J. Chem. Theory Comput. **19**, 5151 (2023).

[38] A. Bochkarev, Y. Lysogorskiy, C. Ortner, G. Csányi, and R. Drautz, Multilayer atomic cluster expansion for semilocal interactions, Phys. Rev. Res. **4**, L042019 (2022).

[39] G. Dusson, M. Bachmayr, G. Csányi, R. Drautz, S. Etter, C. van der Oord, and C. Ortner, J. Comput. Phys. **454**, 110946 (2022).

[40] R. Drautz, Phys. Rev. B **102**, 024104 (2020).

[41] A. P. Thompson, H. M. Aktulga, R. Berger, D. S. Bolintineanu, W. M. Brown, P. S. Crozier, P. J. in 't Veld, A. Kohlmeyer, S. G. Moore, T. D. Nguyen, R. Shan, M. J. Stevens, J. Tranchida, C. Trott, and S. J. Plimpton, Comput. Phys. Commun. **271**, 108171 (2022).

[42] A. H. Larsen, J. J. Mortensen, J. Blomqvist, I. E. Castelli, R. Christensen, M. Dułak, J. Friis, M. N. Groves, B. Hammer, C. Hargus *et al.*, J. Phys.: Condens. Matter **29**, 273002 (2017).

[43] A. Togo and I. Tanaka, Scr. Mater. **108**, 1 (2015).

[44] S. Menon, Y. Lysogorskiy, J. Rogal, and R. Drautz, Phys. Rev. Mater. **5**, 103801 (2021).

[45] D. Frenkel and A. J. Ladd, J. Chem. Phys. **81**, 3188 (1984).

[46] M. de Koning, A. Antonelli, and S. Yip, Phys. Rev. Lett. **83**, 3973 (1999).

[47] M. de Koning, A. Antonelli, and S. Yip, J. Chem. Phys. **115**, 11025 (2001).

[48] J. Janssen, S. Surendralal, Y. Lysogorskiy, M. Todorova, T. Hickel, R. Drautz, and J. Neugebauer, Comput. Mater. Sci. **163**, 24 (2019).

[49] Y. Lysogorskiy, A. Bochkarev, M. Mrovec, and R. Drautz, Phys. Rev. Mater. **7**, 043801 (2023).

[50] G. V. Sin'ko and N. A. Smirnov, Phys. Rev. B **80**, 104113 (2009).

[51] L. J. Slutsky and C. Garland, Phys. Rev. **107**, 972 (1957).

[52] P. Virtanen, R. Gommers, T. E. Oliphant, M. Haberland, T. Reddy, D. Cournapeau, E. Burovski, P. Peterson, W. Weckesser, J. Bright, S. J. van der Walt, M. Brett, J. Wilson, K. J. Millman, N. Mayorov, A. R. J. Nelson, E. Jones, R. Kern, E. Larson, C. J. Carey *et al.*, Nat. Methods **17**, 261 (2020).

[53] S. Kirklin, J. E. Saal, B. Meredig, A. Thompson, J. W. Doak, M. Aykol, S. Rühl, and C. Wolverton, npj Comput. Mater. **1**, 15010 (2015).

[54] R. Tran, X.-G. Li, J. H. Montoya, D. Winston, K. A. Persson, and S. P. Ong, Surf. Sci. **687**, 48 (2019).

[55] H. Zheng, X.-G. Li, R. Tran, C. Chen, M. Horton, D. Winston, K. A. Persson, and S. P. Ong, Acta Mater. **186**, 40 (2020).

[56] G. S. Rohrer, *Structure and Bonding in Crystalline Materials* (Cambridge University Press, Cambridge, 2001).

[57] W. Hutchinson and M. Barnett, Scr. Mater. **63**, 737 (2010).

[58] R. Sánchez-Martín, M. T. Pérez-Prado, J. Segurado, J. Bohlen, I. Gutiérrez-Urrutia, J. Llorca, and J. M. Molina-Aldareguia, Acta Mater. **71**, 283 (2014).

[59] H. Fan and J. A. El-Awady, Mater. Sci. Eng., A **644**, 318 (2015).

[60] J. Geng, M. F. Chisholm, R. Mishra, and K. Kumar, Philos. Mag. Lett. **94**, 377 (2014).

[61] M. Itakura, H. Kaburaki, M. Yamaguchi, and T. Tsuru, Phys. Rev. Lett. **116**, 225501 (2016).

[62] K. Y. Xie, Z. Alam, A. Caffee, and K. J. Hemker, Scr. Mater. **112**, 75 (2016).

[63] B. Yin, Z. Wu, and W. Curtin, Acta Mater. **123**, 223 (2017).

[64] V. Vítek, Philos. Mag. **18**, 773 (1968).

[65] N. Chetty and M. Weinert, Phys. Rev. B **56**, 10844 (1997).

[66] A. E. Smith, Surf. Sci. **601**, 5762 (2007).

[67] I. Shin and E. A. Carter, Modell. Simul. Mater. Sci. Eng. **20**, 015006 (2012).

[68] L. Wen, P. Chen, Z.-F. Tong, B.-Y. Tang, L.-M. Peng, and W.-J. Ding, Eur. Phys. J. B **72**, 397 (2009).

[69] Y. Wang, L.-Q. Chen, Z.-K. Liu, and S. Mathaudhu, Scr. Mater. **62**, 646 (2010).

[70] J. Zhang, Y. Dou, G. Liu, and Z. Guo, Comput. Mater. Sci. **79**, 564 (2013).

[71] R. Smallman and P. Dobson, Metall. Trans. **1**, 2383 (1970).

[72] D. Sastry, Y. Prasad, and K. Vasu, Scr. Metall. **3**, 927 (1969).

[73] A. Couret and D. Caillard, Acta Metall. **33**, 1455 (1985).

[74] J. A. Yasi, Jr, T. Nogaret, D. Trinkle, Y. Qi, L. Hector, and W. Curtin, Modell. Simul. Mater. Sci. Eng. **17**, 055012 (2009).

[75] M. Ghazisaeidi, L. G. Hector Jr, and W. Curtin, Scr. Mater. **75**, 42 (2014).

[76] A. Ready, P. Haynes, D. Rugg, and A. Sutton, Philos. Mag. **97**, 1129 (2017).

[77] N. Chaari, E. Clouet, and D. Rodney, Metall. Mater. Trans. A **45**, 5898 (2014).

[78] R. Freitas, M. Asta, and M. De Koning, Comput. Mater. Sci. **112**, 333 (2016).

[79] R. M. Wentzcovitch and M. L. Cohen, Phys. Rev. B **37**, 5571 (1988).

[80] E. Ibrahim, Atomic cluster expansion for a general-purpose interatomic potential of magnesium, Zenodo (2023); doi: 10.5281/zenodo.10021807.